OMI-observed HCHO in Shanghai, China during 2010-2019 and ozone sensitivity inferred by improved HCHO/NO₂ ratio

Danran Li [1], Shanshan Wang [1,2], Ruibin Xue [1], Jian Zhu [1], Sanbao Zhang[1], Zhibin Sun[1], and Bin Zhou [1,2,3]

[1]Shanghai Key Laboratory of Atmospheric Particle Pollution and Prevention (LAP[3]), Department of Environmental Science and Engineering, Fudan University, Shanghai, China
[2]Institute of Eco-Chongming (IEC), No. 20 Cuiniao Road, Shanghai 202162, China
[3]Institute of Atmospheric Sciences, Fudan University, Shanghai, 200433, China

Correspondence to: Shanshan Wang (shanshanwang@fudan.edu.cn)

Abstract. In recent years, satellite remote sensing has been increasingly used in the long-term observation of ozone (O_3) precursors and its formation regime. In this work, formaldehyde (HCHO) data from Ozone Monitoring Instrument (OMI) were used to analyse the temporal and spatial distribution of HCHO vertical column densities (VCDs) in Shanghai from 2010 to 2019. HCHO VCDs exhibited the highest value in summer and the lowest in winter, the high-VCD concentrated in western Shanghai. Temperature largely influence HCHO by affecting the biogenic emissions and photochemical reactions, and industry was the major anthropogenic source. The satellite observed formaldehyde to nitrogen dioxide ratio (FNR_{SAT}) reflects that the O_3 formation regime had significant seasonal characteristics and gradually manifested as transitional ozone formation regime dominated in Shanghai. The uneven distribution in space was mainly reflected as the higher FNR_{SAT} and surface O_3 concentration in suburban area. To compensate the shortcoming of FNR_{SAT} that it can only characterize O_3 formation around satellite overpass time, correction of FNR_{SAT} was implemented with hourly surface FNR and O_3 data. After correction, O_3 formation regime showed the trend moving towards VOC-limited in both time and space, and regime indicated by FNR_{SAT} can better reflect O_3 formation for a day. This study can help us better understand HCHO characteristics and O_3 formation regime in Shanghai, and also provide a method to improve FNR_{SAT} for characterizing O_3 formation in a day, which will be significant for developing O_3 prevention and control strategies.

1 Introduction

Formaldehyde (HCHO) is an important trace gas in atmosphere. It has the irritating effect on human eyes, skin, and respiratory mucosa, and can also cause cancer in high concentration (Zhu et al., 2017a; Liu et al., 2018a). Atmospheric HCHO is an intermediate product of almost all volatile organic compounds (VOCs) oxidation, it can be therefore indicative of the overall VOCs level (Chan et al., 2019). HCHO can also be emitted through anthropogenic sources, biogenic sources, and biomass combustion. Anthropogenic sources like transportation, power, industry, and residential etc. increase the amount of HCHO by emitting VOCs into the atmosphere (Wang et al., 2017). In addition, biogenic volatile organic

compounds (BVOCs) are also important sources of HCHO. Isoprene emitted by plant can be oxidized to generate HCHO, which causes the concentration of HCHO in some lush vegetation areas to be largely affected by emission of BVOCs (Millet et al., 2008). The removal of HCHO is mainly through photolysis, reaction with OH radicals and the deposition (Ling et al., 2016; Xing et al., 2020).

35 Satellite remote sensing can achieve large-scale observation of atmospheric pollutant gases including HCHO, which has been widely used in recent years. Sensors currently available for HCHO observation include the Global Ozone Monitoring Experiment (GOME) on ERS-2 (Burrows et al., 1999; Martin et al., 2004b), Scanning Imaging Absorption Spectrometer for Atmospheric Chartography (SCIAMACHY) on ENVISAT (Bovensmann et al., 1999; Stavrakou et al., 2009), Ozone Monitoring Instrument (OMI) on Aura (Levelt et al., 2006; Zhu et al., 2017b), GOME-2 A, B, and C on METOP as the

40 successor of GOME (Callies et al., 2000; De Smedt et al., 2012), Ozone Mapping and Profiler Suite (OMPS) on Suomi-NPP (Su et al., 2019), and Tropospheric Monitoring Instrument (TROPOMI) on Sentinel-5P (Veefkind et al., 2012; Vigouroux et al., 2020). OMI can provide daily data of HCHO with higher spatial resolution (13 km×24 km). As a new generation of sensors, TROPOMI was launched in 2017, it has better spatial resolution (7 km×7 km) but lacks long-term observation so far. It would be an advantageous tool of satellite remote sensing to achieve more detailed analysis in the future (Veefkind et al.,

45 2012).

Previous studies reported satellite observed long-term and large-scale distribution and variation of HCHO in China and all over the world (Millet et al., 2008; Zhu et al., 2017a; Liu et al., 2020). Twelve years observation of multi-satellite (OMI, GOME-2, SCIAMACHY) showed that the trend of HCHO vertical column densities (VCDs) over eastern China is consistent with that of anthropogenic VOCs (Shen et al., 2019). Based on 10 years observation of OMI HCHO, Liu et.al

50 (2018a) indicated that high HCHO VCDs in tropical forests region are greatly affected by biomass burning and meteorological factors including temperature and precipitation. In addition, the ground-based remote sensing can also be available for HCHO observation, such as the multi axis differential optical absorption spectroscopy (MAX-DOAS) measurement. The vertical distribution of HCHO derived from MAX-DOAS measurement was characterized by the higher HCHO concentrated near the surface (Lee et al., 2015; Chan et al., 2019). By employing the box model, Li et al. (2014)

55 found that isoprene oxidation initiated by OH radicals have a great contribution to the HCHO formation in semi-rural region of the Pearl River Delta (PRD) in China.

HCHO participates in the complex photochemical reaction of NO_x (NO_x= NO + NO_2) and directly affects the production of O_3 in troposphere. Due to the short lifetime of HCHO and NO_2, their spatial distributions were greatly affected by local emission of VOCs and NO_x, which received widespread attention as precursors of tropospheric O_3 (Zaveri et al., 2003; Chan

60 et al., 2019). Consequently, HCHO and NO_2 can be assumed as indicators of VOCs and NO_x, and the ratio of formaldehyde to nitrogen dioxide (HCHO/NO_2, FNR) can be an indicator to analyse the O_3 formation regime (Sillman, 1995; Martin et al., 2004a; Schroeder et al., 2017). For instance, by using FNR from long-term OMI HCHO and NO_2 data, O_3 sensitivity of the United States was evaluated. O_3 formation regime can be designated as VOC-limited for FNR < 1, NO_x-limited for FNR > 2, and transition for 1 < FNR < 2, which serves as the transitional regime between VOC-limited and NO_x-limited regimes,

65 indicating the production of O_3 can be changed by both VOC and NO_x (Duncan et al., 2010). In view of China, OMI products over three representative regions (North China Plain (NCP), the Yangtze River Delta (YRD) and the PRD) were investigated, revealing that the O_3 formation regime varied in both time and space, and the contribution of emission sectors to precursors changed with the type of regimes (Jin and Holloway, 2015). During special events such as Asia-Pacific Economic Cooperation in 2014 and Grand Military Parade in 2015, FNR in Beijing had become higher compared with

70 previous periods, and the O_3 formation regime shifted toward NO_x-limited regime with control strategies (Liu et al., 2016). In this study, OMI satellite data were used to investigate the temporal and spatial distribution characteristics of atmospheric HCHO in Shanghai from 2010 to 2019, combined with meteorological data and emission inventories to analyse the influencing factors. FNR calculated by satellite HCHO and NO_2 were applied to capture variation of the O_3 formation regime in Shanghai over the past decade. Considering that satellite data only reflect the column density of trace gas around overpass

75 time, hourly surface FNR and O_3 concentration increment were proposed to correct the satellite FNR, so that it can better indicate O_3 formation in the daytime.

2 Data and Methods

2.1. Satellite data

OMI on Aura orbits the earth in about 98 minutes, which can achieve full coverage of the earth in one day. It overpasses at

80 13:45 local time (LT) each day. The scanning width is 2600 km, and is divided into 60 rows. The sensor contains 3 channels, including UV-1, UV-2, and VIS, with a wavelength coverage of 264-504 nm. This band allows to observe a variety of trace gases, e.g., HCHO, NO_2, and SO_2 (Zhang et al., 2019). The retrieval algorithm of this product is based on nonlinear least-squares fitting which get slant column density (SCD) as the result. Then SCD can be converted to VCD through Air Mass Factors (AMF). The Level-2 OMI HCHO product OMHCHO Version-3 is used in this study (https://disc.gsfc.nasa.gov).

85 Since atmospheric HCHO is mainly distributed in the troposphere, the total VCD can be regarded as the tropospheric VCD of HCHO (Duncan et al., 2010). The Level-2 OMI NO_2 product OMNO2.003 Version-4 is adopted as tropospheric NO_2 VCD in this study (https://disc.gsfc.nasa.gov).

2.2. Methodology

In this study, Shanghai and surrounding areas were gridded into to a spatial resolution of 0.01°×0.01°, then HCHO VCD of

90 each pixel was assigned to the respective grid by determining the coordinates information. Weight function including cloud function and pixel size was introduced to effectively improve the quality of processed data (Xue et al., 2020). In order to remove data with poor quality as much as possible, HCHO data with cloud fraction ≤ 30%, solar zenith angle ≤ 70°, and Main Data Quality Flag = 0 were selected in this study. In addition, the quality of pixel data with large size is poor, so 5 marginal pixels on each side were abandoned, and only pixel data within 6~55 were selected (Zhu et al., 2017a; Xue et al.,

95 2020). Because OMI has experienced row anomaly since 2007, Xtrack flag = 0 was required to eliminate the influence of

poor quality data affected by row anomaly (http://projects.knmi.nl/omi/research/product/rowanomaly-background). As HCHO satellite data have large error, fitting root mean square (RMS) ≤ 0.003 was limited to remove most outliers (Souri et al., 2017). The selection of NO_2 satellite data was basically the same as that of HCHO, but without fitting RMS parameter filtering, and cloud radiance fraction ≤30% was required (Krotkov et al., 2016). Moreover, the linear regressions of monthly deseasonalized zonal mean HCHO VCDs with 0.5° latitude steps over remote pacific region (29° - 33 °N, 160° - 140 °W) indicated that OMI HCHO product used in this study do not show the obvious drift (Zhu et al., 2017b).

2.3. Auxiliary data

The meteorological data, including monthly temperature, sunshine hours, precipitation, and relative humidity are acquired from the National Bureau of Statistics of China (http://www.stats.gov.cn/). Hourly temperature data at Shanghai Hongqiao INTL Site (31.20°N, 121.34°E) come from the National Climatic Data Center (NCDC, https://www.ncdc.noaa.gov/). The anthropogenic sources of HCHO in Shanghai are calculated based on the Multi-resolution Emission Inventory for China (MEIC, http://www.meicmodel.org/). Surface HCHO and NO_2 concentrations were measured by long-path differential optical absorption spectroscopy (LP-DOAS) at the Jiangwan campus of Fudan University in Shanghai (31.34°N, 121.52°E). The O_3 data of Qingpu Dianshan Lake Site (31.09°N, 120.98°E) and Hongkou Site (31.30°N, 121.47°E) in Shanghai are obtained from the Shanghai Environmental Monitoring Center (http://www.semc.com.cn/aqi/Home/Index).

3. Results and Discussion

3.1. The temporal and spatial variation of HCHO

HCHO VCDs for annual, monthly and seasonal variations in Shanghai from 2010 to 2019 are shown in Fig. 1. HCHO VCDs decreased from the highest value of 12.29×10^{15} molec·cm^{-2} in 2010 to the lowest value of 9.97×10^{15} molec·cm^{-2} in 2012, then rebounded from 2012 to 2014, and fluctuated slightly in the following years (Fig. 1a). The column value and variation are similar to previous study in the YRD, China (Zhang et al., 2019). Before 2018, the high-VCD concentrated in June to August for about 15×10^{15} to 20×10^{15} molec·cm^{-2}, the low-VCD appeared in January to February and November to December for about 3×10^{15} to 9×10^{15} molec·cm^{-2}, and VCDs were comparable in remaining months (Fig. 1b). In addition, the amplitude of monthly HCHO VCDs was relatively smaller in 2018 and 2019, and mainly concentrated from 6×10^{15} to 15×10^{15} molec·cm^{-2}. The HCHO VCDs varied with the season, the maxima and minima corresponding to the respective summer (June, July and August) and winter (December, January and February), whereas moderate levels in spring (March, April and May) and autumn (September, October and November) (Fig. 1c). Previous MAX-DOAS and OMI observations also exhibited the same seasonal patterns of HCHO in the YRD, China (Jin and Holloway, 2015; Chan et al., 2019). High temperature and abundant radiation are conducive to the plant growth to produce BVOCs and the photochemical reaction of VOCs, which boost the HCHO formation in summer (Sharkey and Loreto, 1993; Duncan et al., 2009; Narumi et al., 2009). Thus, HCHO VCDs would be relatively low in winter under the opposite weather conditions.
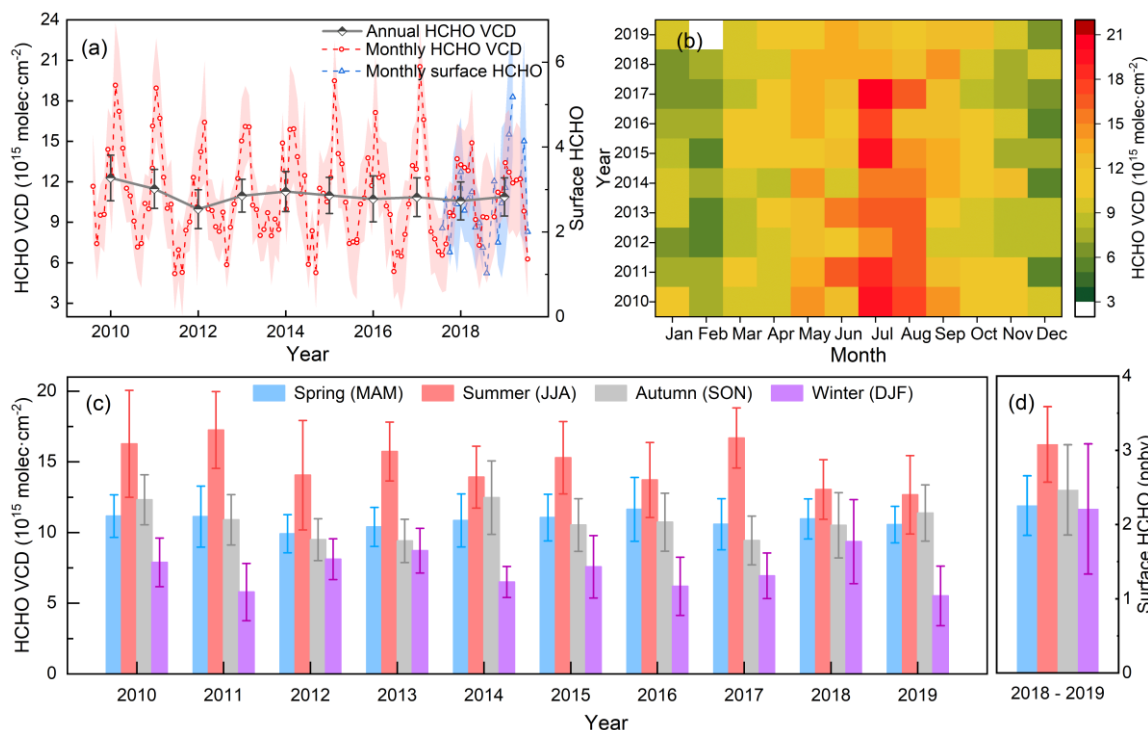
Figure 1. OMI and LP-DOAS observed time series of HCHO in Shanghai. (a) to (c) reflect the annual, monthly and seasonal variations of HCHO VCD during 2010-2019, (d) reflects the seasonal variation of surface HCHO during 2018-2019.

130   The HCHO VCDs within 10 km of LP-DOAS measurement site were averaged to compare with the surface HCHO between 13:00 and 14:00 (Fig. S1). It shows that HCHO VCDs and surface HCHO concentrations are not consistent very well, as HCHO is not completely concentrated near the ground, but has a high concentration at higher altitudes (Chan et al., 2019; Wang et al., 2019). Spatial heterogeneity of surface HCHO in horizontal can also impact the consistency of the comparison. However, the surface HCHO observed by LP-DOAS shows the same seasonal characteristics as HCHO VCDs (Fig. 1d).

135   The spatial distribution of 10-year averaged HCHO VCD was given in Fig. 2a. In general, HCHO VCDs in eastern coastal area were relatively low, with the level of about 10×10^{15} molec·cm^{-2}. While those in western regions adjacent to other provinces were relatively higher, about 13×10^{15} molec·cm^{-2}. Noted that area with the highest HCHO VCD in Shanghai not appeared in the city center (marked by the red box) but in the relatively remote Qingpu (QP) district, followed by Songjiang (SJ) and Jinshan (JS) district. Compared to the anthropogenic Non-methane volatile organic compounds (NMVOCs)

140   emissions, the distribution of HCHO VCDs does not show the same spatial pattern (An et al., 2021). The high HCHO in western Shanghai were frequently observed and may be explained by the transport of air masses containing high concentrations of reactive VOCs sometimes from Zhejiang and Jiangsu provinces and the significant contribution of local biogenic isoprene to HCHO (Su et al., 2019; Zhang et al., 2020; Zhang et al., 2021).

Figure 2b shows the difference of HCHO VCDs between 2019 and 2010. It suggests that except for the eastern and southern

145   coastal areas, as well as the eastern area of Chongming Island, HCHO VCDs in Shanghai showed an overall downward trend

during the past 10 years, with Qingpu district experiencing the largest decline. Figure 2c to Fig. 2f display the spatial distribution of HCHO VCDs in different seasons. HCHO VCD in summer was basically above 12×10^{15} molec·cm^{-2}. In winter, the value was around 7×10^{15} molec·cm^{-2} for most regions except for Qingpu district. While in spring and autumn, it was in the moderate level of about 10×10^{15} molec·cm^{-2}. The spatial distribution of HCHO VCDs in different seasons was

150 similar to the 10-year averaged characteristics of high-value in the west and low-value in the east.
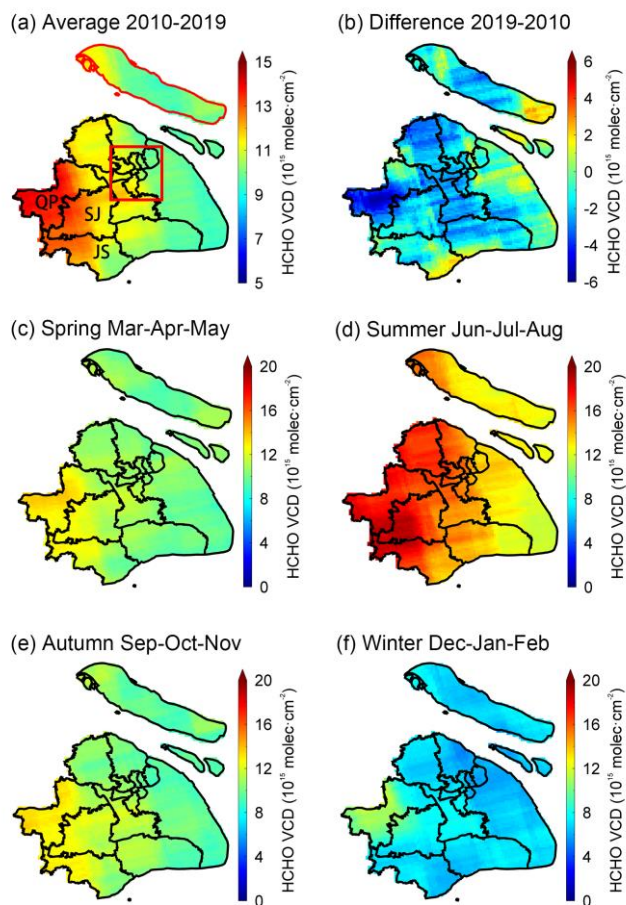
Figure 2. Spatial distribution of HCHO VCDs in Shanghai: (a) average HCHO VCD for 10 years, (b) the difference of HCHO VCDs between 2019 and 2010 (2019 minus 2010), and (c) to (f) for different seasons. In Fig. 2a the city center is marked with red box, Chongming Island is displayed with red boundary, QP, SJ, and JS refer to Qingpu, Songjiang, and Jinshan district.

155 **3.2. Influencing factors**

The relationship between monthly HCHO VCDs and meteorological variables including temperature, sunshine hours, precipitation, and relative humidity were analysed via the linear regression. The stepwise regression results show that only temperature correlated with HCHO VCDs significantly among these four meteorological factors. The linear regression of temperature contribution and HCHO VCD was shown in Fig. 3. The temperature contribution has a good correlation with the

160   observed HCHO VCD ($R^2 = 0.72$), which means that temperature can explain about 72% of the variation of HCHO VCD. The remaining part that cannot be explained by temperature appears in the form of residual, which is considered as the influence of other changing factors such as anthropogenic emissions (Li et al., 2019). The residual in summer in some years would be particularly large, which indicates that in addition to temperature, there are other factors affecting HCHO VCD significantly.

165
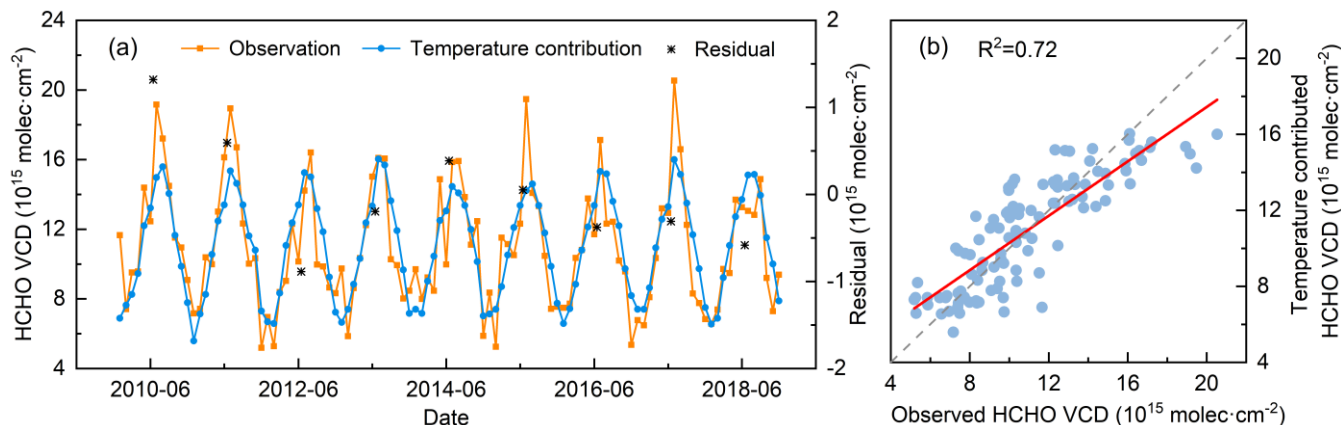
Figure 3. Monthly HCHO VCDs and the temperature contribution in Shanghai during 2010-2018. (a) reflects the temporal variations and (b) illustrates the correlation analysis. The black points represent the annual average residuals.

170   The precipitation and relative humidity reached peak in June, while the sunshine hours reached the dip, and HCHO VCD declined with the temperature rose (Fig. S2). Shanghai has a subtropical monsoon climate with rain and heat in the same period. Abundant precipitation largely favoured the wet deposition of HCHO and offset the impact of rising temperature, resulting in a small decrease in HCHO VCDs in June (Pang et al., 2009). The result of Fisher's exact test also illustrates that when the relative humidity changes remarkably, the variation of HCHO VCDs in summer would be significantly affected (P

175   <0.05).

   To explore the impacts of anthropogenic sources on HCHO abundance, primary emissions and secondary productions of HCHO from anthropogenic sources were estimated. NMVOCs emissions from MEIC v.1.3 grid inventories for the year of 2010, 2012, 2014, and 2016 were mapped to SAPRC07 mechanism species. Primary HCHO was directly obtained from the inventory, secondary HCHO production was calculated based on 1-day HCHO yields of several NMVOCs under high-NO_x

180   condition (Table S1) (Shen et al., 2019).
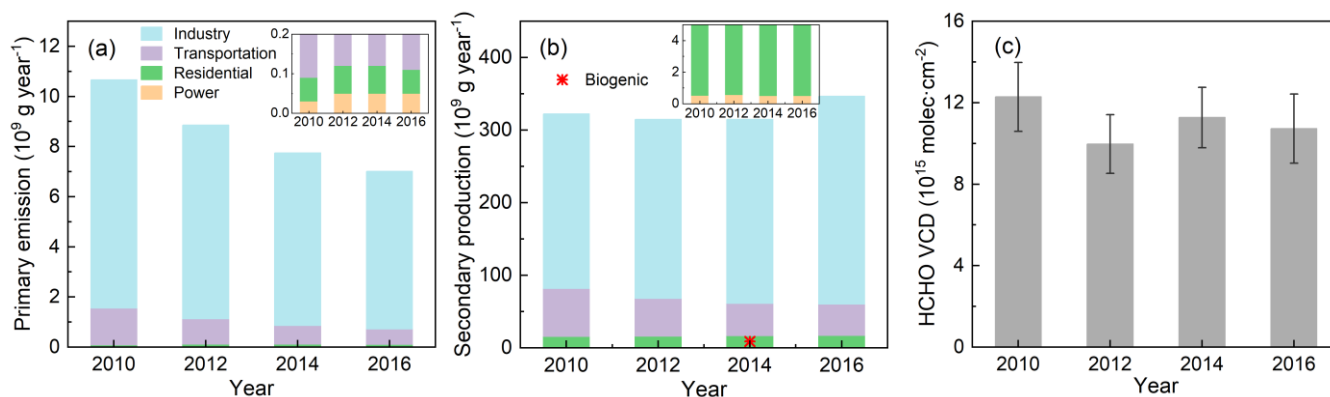
Figure 4. Primary and estimated secondary production of HCHO from anthropogenic NMVOCs, biogenic contribution of HCHO in 2014 was marked as red cross in Figure 4(b).

185

In Fig. 4a and 4b, for the total of primary emissions and secondary productions, the contribution of industrial sector was much higher than other sectors, accounting for about 79.3% of the total, followed by transportation sector, accounting for about 15.7%. Residential and power sectors were far lower, the proportions over these years were basically less than 5%. As major sectors, the contribution of industrial increased 17.2%, while the contribution of transportation decreased about

190 35.2%. The primary emission of HCHO keeps decreasing (about 34.2% compared to 2010), while secondary produced HCHO did not change significantly. Furthermore, the changes and proportional relationships between primary emission and secondary production of HCHO for these sectors are different, which means the VOCs source profile of different emission sectors would affect the amount of secondary HCHO production.

In addition, HCHO produced by biogenic sources in 2014 was also calculated, and the BVOCs emissions were referred from

195 Liu et al. (Liu et al., 2018b; 2018c). HCHO yield from BVOCs emission was about 9.07×10^9 g, which is much smaller compared with anthropogenic contribution, indicating that the anthropogenic is the main contributor of secondary production of HCHO in Shanghai (Shen et al., 2019; Fan et al., 2021).

Fig. 4c shows that the annual trend of HCHO VCDs is not synchronized with that of primary or secondary HCHO. It means that, besides the combined effect of the primary and secondary source, the changes of HCHO VCDs should also be affected

200 complexly by various factors. In addition, it should be noted that HCHO yield from VOCs is proportional to NO_x condition (Palmer et al., 2006; Marais et al., 2012; Miller et al., 2017). With context of the continuous NO_x decreases in Shanghai, the estimation using a fixed HCHO yield may overestimate secondary HCHO production in later years (Xue et al., 2020). However, the NO_x concentration in Shanghai (basically 30-60 ppbv in urban) is still much higher than the defined high NO_x condition (1 ppbv) in previous studies (Gao et al., 2017). Therefore, in such a high NO_x condition, the effect of NO_x

205 decreases on HCHO yield needs to be further studied.

3.3. FNR and O₃ formation regime

As the important precursors of O_3, HCHO and NO_2 can be served as indicators for VOCs and NO_x. On this basis, the HCHO/NO₂ ratio from satellite observation (FNR_{SAT}) can be employed to identify the O_3 formation regime. The variations of monthly averaged VCDs of HCHO, NO_2, and FNR_{SAT} in Shanghai over the past 10 years are given in Fig. 5. NO_2 VCDs were featured by the highest in winter and the lowest in summer, which was opposite to HCHO and fluctuated more fiercely. The peaks were mainly on account of its longer lifetime in winter (Zhang et al., 2007). While in summer, the adequate sunlight and precipitation accelerated the photochemical removal and wet deposition of NO_2, resulting in the dip (Wang et al., 2018; Xue et al., 2020). FNR_{SAT} also exhibited the obvious annual cycle of high in summer and low in winter. According to the criteria proposed by Duncan et.al (2010), O_3 formation regime in Shanghai was usually under NO_x-limited from June to August, and controlled by VOC-limited and transition regime for the rest of months. From May to September in 2014, Shanghai all under NO_x-limited regime, and FNR_{SAT} reached the highest value over the past 10 years. In 2019, the value of monthly FNR_{SAT} fluctuated gently, which showed the trend moving towards the transition regime threshold of 1-2.
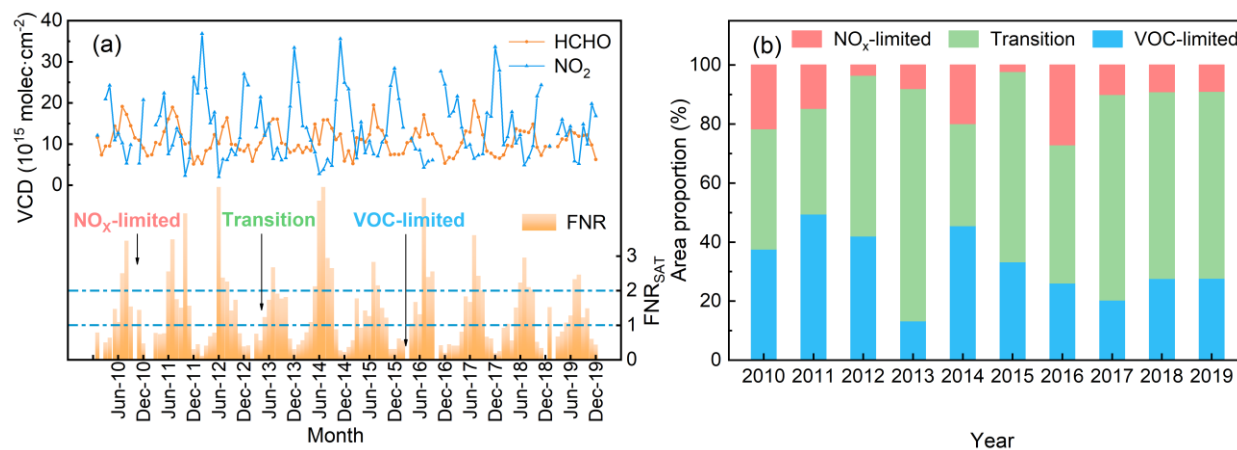
Figure 5. Temporal and spatial variation of FNR$_{SAT}$ in Shanghai: (a) variations of HCHO, NO₂ and FNR$_{SAT}$ from 2010 to 2019, and (b) the area proportion for different O₃ formation regimes in these years.

The spatial distribution of FNR_{SAT} in Shanghai is presented in Fig. 6. Comparing FNR_{SAT} in 2019 with that in 2010, the NO_x-limited regime in the western Shanghai transformed into transition regime, and VOC-limited regime in the northern Chongming Island almost completely became transition regime. It manifests itself in the reduction in the NO_x-limited and VOC-limited regimes while the increase in the transition regime. Referring to previous study on the variation of NO_2 VCDs spatial distribution in Shanghai observed by satellite, this phenomenon may be related to the spatial characteristics of concentration variations of two precursors (Xue et al., 2020). This result is also reflected in Fig. 5b. In the past 10 years, the proportion decreased from 37.6% to 27.7% for VOC-limited area, and from 21.6% to 8.9% for NO_x-limited area, respectively. Meanwhile, the transition regime area increased from 40.8% to 63.3%. Xu et al. (2019) suggested that O_3 formation regime in Shanghai trend to transform from VOC-limited regime to NO_x-limited regime after 2020 through WRF-

230 Chem model simulation. In this study, the increase of transition regime may be the transition state from VOC-limited to NO$_x$-limited regime.
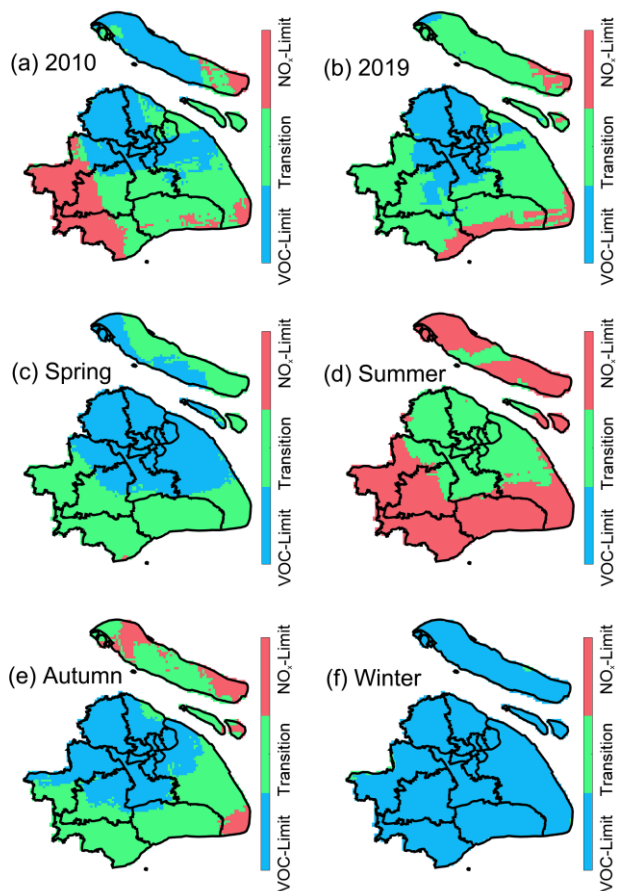
Figure 6. The spatial distribution of FNR$_{SAT}$ for (a) 2010, (b) 2019, and (c) to (f) different seasons in Shanghai.

Figure. 6c to Fig. 6f show the spatial distribution of FNR$_{SAT}$ for different seasons during the decade. In spring, the northern
235 area of Shanghai was VOC-limited regime while the southern area was transition regime. From spring to summer, the VOC-limited area almost transformed into transition regime, and the transition regime nearly turned into NO$_x$-limited at the same time, which mainly caused by the increase of HCHO and the decrease of NO$_2$. The distribution in autumn was similar to that in spring. In winter, Shanghai was basically under VOC-limited. In the light of the temporal and spatial distribution of O$_3$ formation regime inferred by FNR$_{SAT}$, the emission reduction measures for O$_3$ precursors would be more rationally.

240 Besides, there are differences in O$_3$ formation regime in urban and suburban areas of Shanghai, with the main manifestation that the central urban area was inclined to be in VOC-limited regime and the suburban area was more likely to be in NO$_x$-limited regime. In order to analyse the differences in more detail, area within 10 km around the Jiangwan campus of Fudan University was selected to represent the urban area (about 12 km to the city center), and equally sized area around Dianshan Lake (31.09°N, 120.98°E) of Qingpu district was regarded as the suburban area (about 50 km to the city center), respectively.

245 Since O$_3$ pollution is relatively serious from April to September, this period can be chosen as a research case. The maximum 8-hour average concentration of O$_3$ at the Hongkou and the Qingpu Dianshan Lake Site were used to characterize O$_3$ concentration in urban and suburban areas. NO$_2$ VCDs in urban area were higher than that in suburban, while HCHO VCDs presented the opposite character (Fig. 7a). The lower NO$_2$ in suburban area was associated with the less NO$_x$ emission than that in urban, corresponding to the larger FNR$_{SAT}$. From Fig. 7b, the O$_3$ production was under transition regime in suburban
250 area except for 2016, while VOC-limited regime occupied for most years in urban area. The O$_3$ concentration in suburban area was always higher than that in urban (Fig. 7c). In this study, transition regime in suburban for most years led to higher O$_3$ concentration correspondingly (Jin et al., 2020). In addition, high concentration of NO$_x$ in urban area may lead to titration of O$_3$ by NO, which would also cause the lower O$_3$ concentration in urban (Geng et al., 2008; Duncan et al., 2010).
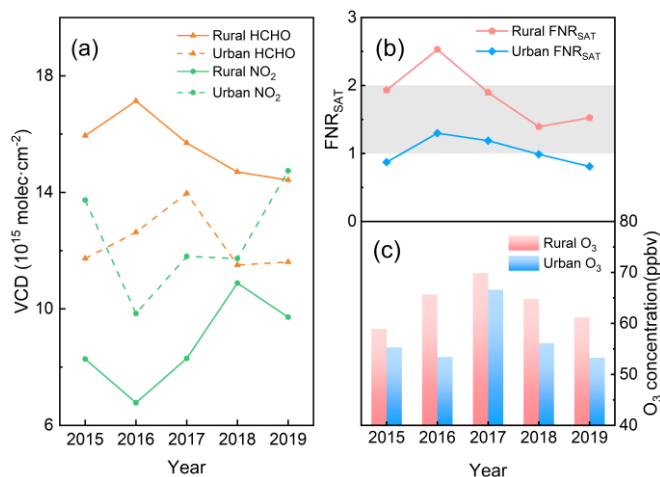
255 **Figure 7. Differences of (a) satellite observation of HCHO and NO$_2$ VCDs, (b) FNR$_{SAT}$ and (c) surface O$_3$ concentration in urban and suburban areas of Shanghai from 2015 to 2019.**

3.4. Correction of FNR$_{SAT}$

FNR is originally proposed as an indicator to characterize the sensitivity of the instantaneous O$_3$ production rate (Duncan et al., 2010). Satellite observation only reflects the averaged column of the trace gases around overpass time, so the FNR$_{SAT}$
260 may not accurately infer the surface O$_3$ formation regime during the day (Duncan et al., 2010; Jin and Holloway, 2015; Jin et al., 2017). FNR$_{SAT}$ was compared with FNR$_{LP}$ at the satellite overpass time on the monthly and daily scales. Results show that FNR$_{SAT}$ and FNR$_{LP}$ were consistent well on monthly scale (R^2=0.95, between April and August), but they were quite different on the daily scale, and the relationship was easily affected by the boundary layer height (BLH) and other factors (Schroeder et al., 2017).
265 As shown in Fig. 8a to Fig.8c, LP-DOAS observation provided FNR$_{LP}$ with the high temporal resolution throughout the day, and FNR$_{LP}$ was in good agreement with hourly O$_3$ concentration. It means that FNR$_{LP}$ should be a good indicator to distinguish the formation regime of surface O$_3$ on a detailed time scale. In addition, the highest value of FNR$_{LP}$ at noon

means that FNR$_{SAT}$ at overpass time approximately close to the highest level in a day. Thus, it would be valuable to introduce the time series of FNR$_{LP}$ to make FNR$_{SAT}$ better reflect the characteristic of O$_3$ formation during the daytime.

270
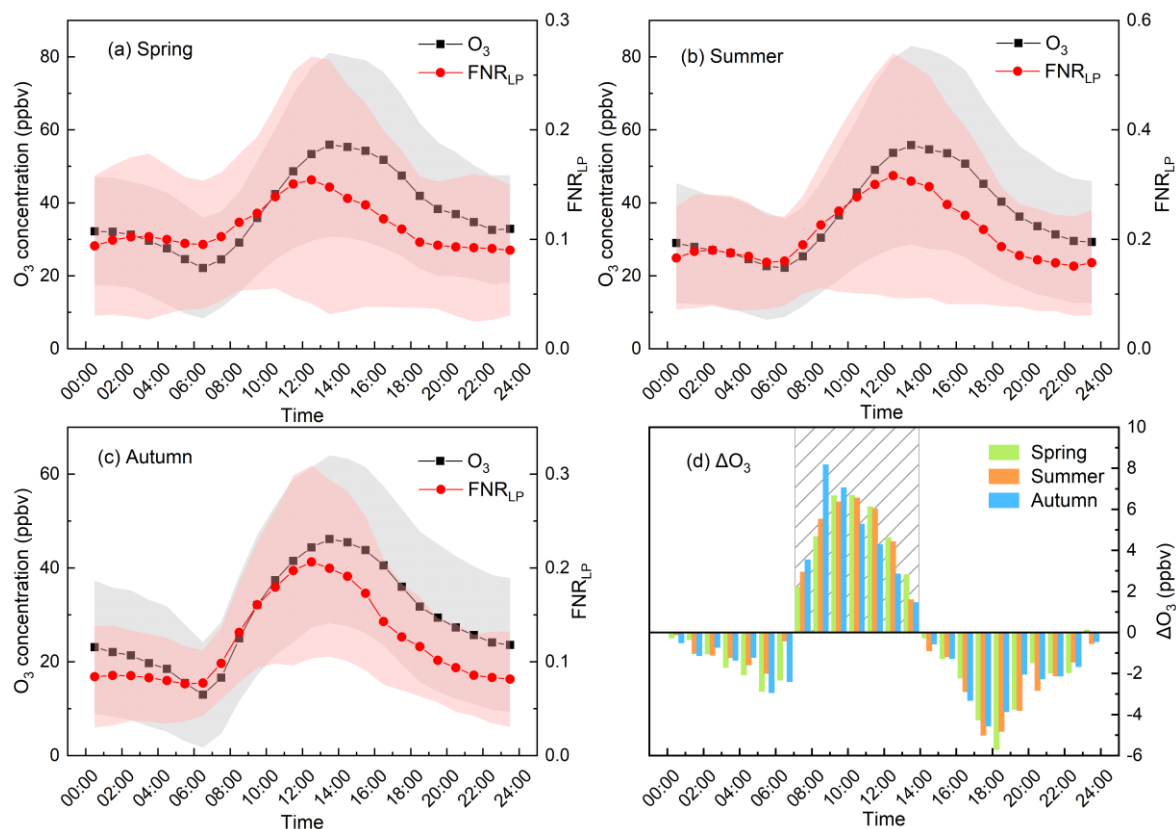
Figure 8. Diurnal variations of FNR$_{LP}$, O$_3$ and ΔO$_3$ for spring, summer and autumn during 2018-2019. ΔO$_3$ represents increment of hourly O$_3$ concentration, as referred to Eq. (3). The shaded area in (d) represents the period when ΔO$_3$ greater than 0.Three cases during the LP-DOAS observation at the Jiangwan campus of Fudan University were selected for the

275 further discussion under the criteria of the hourly concentration of O$_3$ exceeding 200 μg/m^3 (secondary concentration limit stipulated in ambient air quality standards of China, GB 3095-2012). In Fig. 9a and Fig. 9c, the upward trend in FNR$_{LP}$ as the O$_3$ concentration increases means that the formation of O$_3$ was under VOC-limited regime in Case 1 and 3. VOC-limited and transition regimes caught in Case 1 through FNR$_{SAT}$ were different from that identified by FNR$_{LP}$. In Case 3, the O$_3$ formation regime remained in VOC-limited regime, which was the same as FNR$_{LP}$. As shown in Fig. 8b, FNR$_{LP}$ indicated

280 that the O$_3$ formation regime switched between three regimes in Case 2. As O$_3$ concentration increasing, the growth of FNR$_{LP}$ at beginning indicated VOC-limited regime, while the subsequent slow variation suggested transition regime. When O$_3$ concentration reached maximum, FNR$_{LP}$ got smaller, which referred to NO$_x$-limited regime. But FNR$_{SAT}$ only captured the VOC-limited and transition regime in Case 2. According to the results above, it is feasible and necessary to correct

FNR$_{SAT}$ to better represent the sensitivity of surface O$_3$ formation. Due to the less O$_3$ pollution in winter, FNR$_{SAT}$ was only corrected for the remaining three seasons.
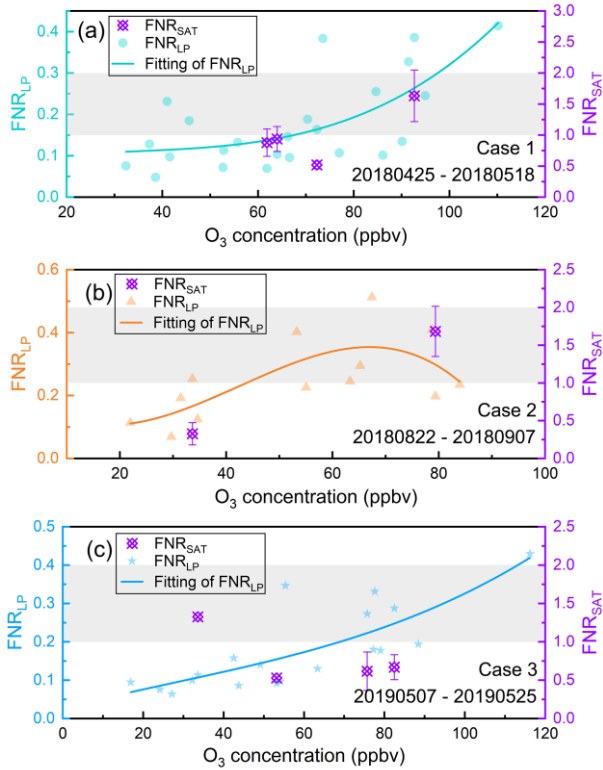
Figure 9. Comparison of FNR$_{SAT}$ and FNR$_{LP}$ in three O$_3$ pollution cases. The curves are polynomial fit of FNR$_{LP}$, and the points are FNR$_{SAT}$ in corresponding cases, the gray area indicates the transition regime for FNR$_{SAT}$. Only LP-DOAS measured data between 08:00-18:00 LT were contained.

The correction of FNR$_{SAT}$ was achieved through the following process. Firstly, the ratio of FNR at satellite overpass time to averaged FNR during O$_3$ pollution period (ΔO$_3$ greater than 0, i.e. 07:00 to 13:00 LT, referred to Fig. 8d) obtained from ground surface measurement was assumed to be same with that of satellite observation, which is expressed as:

$$\frac{FNR_{SAT}}{\overline{FNR}_{SAT}} = \frac{FNR_{LP,overpass\ time}}{\overline{FNR}_{LP}} \qquad (1)$$

where $\overline{FNR}_{LP}$ is weighted average of FNR during O$_3$ pollution period observed by ground surface LP-DOAS measurement, FNR$_{LP,overpass\ time}$ is ground surface FNR observed at satellite overpass time. $\frac{FNR_{LP,overpass\ time}}{\overline{FNR}_{LP}}$ reflects the numerical relationship of FNR between satellite overpassed time and O$_3$ polluted period during a day, and can be serve as the correction coefficient to realize the correction for FNR$_{SAT}$ on time scale to obtain the $\overline{FNR}_{SAT}$. Considering the relationship between time series of FNR and O$_3$ formation, ΔO$_3$ was involved to calculate the weighted average of FNR$_{LP}$ ($\overline{FNR}_{LP}$) during 07:00 to 13:00 LT via Eq. (2), which can better indicate the ozone formation in a day.

$$\overline{FNR}_{LP} = \frac{\sum_{T=7}^{13} FNR_{LP,T} \times \Delta\Omega_{O3,T}}{\sum_{T=7}^{13} \Delta\Omega_{O3,T}} \qquad (2)$$

$$\Delta\Omega_{O3,T} = \Omega_{O3,T} - \Omega_{O3,T-1} \qquad (3)$$

Where $\Delta\Omega_{O3,T}$ is the increase of O_3 concentration at time T, $FNR_{LP,T}$ is the FNR_{LP} at time T. Moreover, variation characteristics of FNR_{LP} in different seasons (as shown in Fig. 8a to Fig. 8c) suggest that the correction of FNR_{SAT} should be discussed seasonally.

Afterwards, the seasonal correction coefficients of 0.85, 0.84, and 0.77 were obtained for spring, summer, and autumn, respectively. It is noted that all the correct coefficients were less than 1 due to the FNR_{LP} value for OMI overpasses time relatively larger than other time. It would inevitably make the O_3 formation regime inferred by corrected FNR_{SAT} trend to be VOC-limited. There were 87 months with effective FNR_{SAT} in three seasons during 2010-2019 and the proportion of months for different regimes was listed in Table 1. Before the correction, the VOC-limited and NO_x-limited regimes, as well as transition regime were almost accounted for about one-third of the total months. After the correction, both of months for VOC-limited and transition regimes increased. The months under VOC-limited regime increased by 25% particularly, while decreased about 32.1% for NO_x-limited regime. Jin et al. (2020) used O_3 exceedance probability as the indicator to analyse non-linear dependence of long-term surface O_3 concentration on precursor emissions, and determined the OMI $HCHO/NO_2$ under transition regime ranging from 3.2 to 4.1. These thresholds are significantly larger than the value proposed by Duncan et al. (2010), which has the equivalent effect as the use of correction factors less than 1 in this study.

Table 1. Variations in the number and proportions of months in 2010-2019 for each regime before and after the correction.

Regime	Before corrected	Percentage before corrected	After corrected	Percentage after corrected	Percentage of change
VOC-limited	28	32.2%	35	40.2%	25.0%
Transition	31	35.6%	33	37.9%	6.5%
NO_x-limited	28	32.2%	19	21.8%	-32.1%

In terms of spatial distribution, the O_3 formation regime after correction in different seasons is shown in Fig. 10. Compared with Fig. 6, part of the transition regime area in spring transformed into VOC-limited regime after the correction, VOC-limited regime obviously expanded and increased about 15.6%. Most area in Chongming Island transformed into VOC-limited regime. In summer, part of the NO_x-limited regime area transformed into transition regime, and the area of transition regime increased about 11.9%. In autumn, the NO_x-limited regime almost disappeared, and the proportion of the transition regime area also decreased significantly, for about 13.2%, while the proportion of the VOC-limited regime area increased about 22%. The O_3 formation regime in Chongming Island was basically under transition regime. Researchers also pointed that thresholds of criteria would be regionally dependent, so the local surface FNR and O_3 concentration should be introduced in satellite correction (Duncan et al., 2010; Jin et al., 2020).
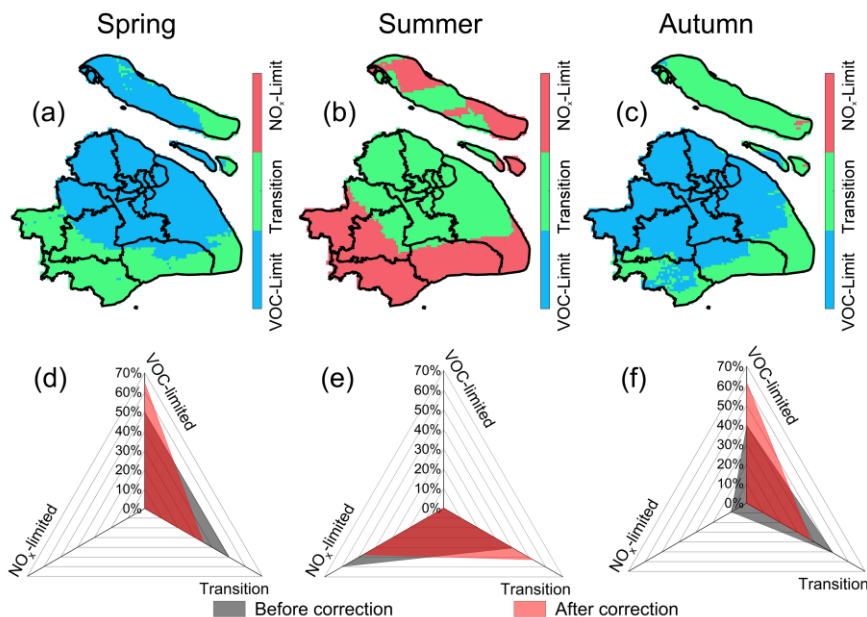
Figure 10. Spatial distribution of O₃ formation regime (upper row) and area proportion for each regime (bottom row) after correction for different seasons in Shanghai during 2010-2019.

330

In order to verify whether the correction of the satellite FNR improved the regime classification, O_3 formation regimes determined by satellite FNR before and after the correction were compared with that of surface observation. The variations of O_3 with surface HCHO and NO_2 have been plotted to determine the O_3 formation regimes from the surface observation (Figure 11). The daytime surface HCHO and NO_2 are from LP-DOAS measurements, and the O_3 observed by SP-DOAS

335 (short-path DOAS), which is also located at Jiangwan campus of Fudan University, have been used with a high temporal resolution. O_3 formation regimes inferred from satellite FNR before and after the correction have also been marked in Figure 11 separately.
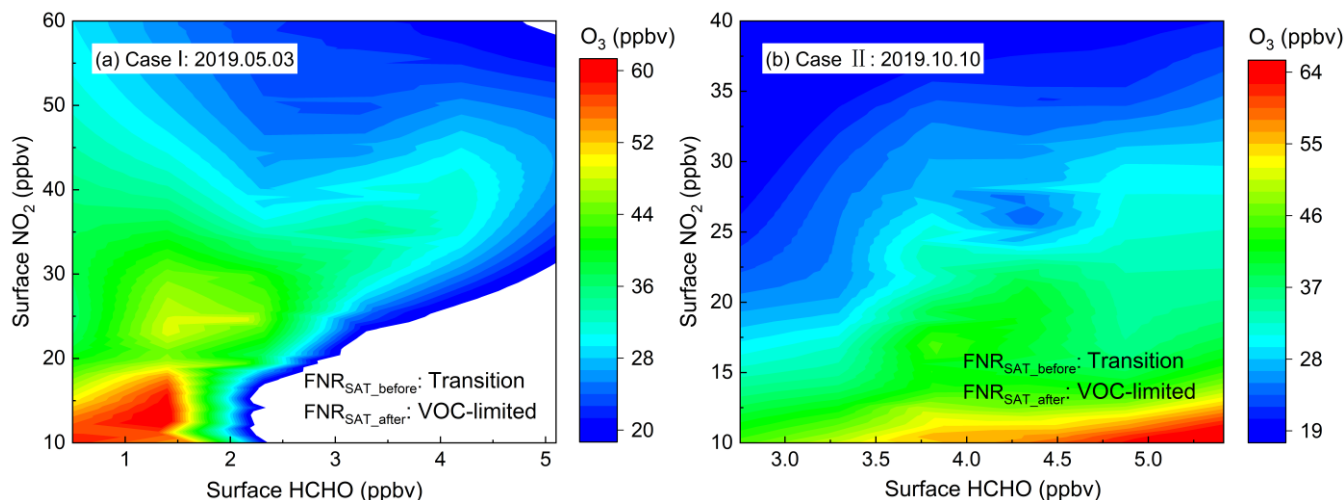
340 **Figure 11. The variation of O₃ with surface HCHO and NO₂ for two cases of (a) May 3th, 2019 and (b) October 10th, 2019. FNR$_{SAT\_before}$ and FNR$_{SAT\_after}$ indicate the O₃ formation regimes inferred from the satellite FNR before and after the correction.**

For Case I, O₃ decreases with the increase of NO₂, which can be attributed to the titration of O₃ by NO (Duncan et al., 2010). O₃ increased from top to bottom indicating it was under VOC-limited regime in Case I (Luo et al., 2020). For Case II, it can

345 be seen that the high O₃ appeared with high HCHO and low NO₂, indicating it was under VOC-limited regime. The uncorrected satellite FNR indicated that these two cases were both under transition regime, while the corrected satellite FNR indicated they transferred to VOC-limited regime, which are consistent with the results of surface observation. It indicates that the correction of FNR$_{SAT}$ in this study can be considered to be effective and make sense.

4. Summary and conclusions

350 Satellite data of OMI were used to study the temporal and spatial variation of HCHO in Shanghai from 2010 to 2019. HCHO VCDs fluctuated during the 10 years with obvious seasonal characteristics of highest value in summer, the lowest value in winter, and the moderate level in spring and autumn. In terms of spatial distribution, HCHO VCDs in western area were much higher than that in eastern coastal area. Compared with 2010, HCHO VCDs of Shanghai in 2019 showed an overall downward trend. As for the influencing factors, temperature give the significant positive effect on HCHO VCDs while the

355 abundant precipitation reduces HCHO in summer. Industry was an important contributor of HCHO, and anthropogenic secondary production of HCHO occupied the main part of the HCHO source.

In the past 10 years, O₃ formation regime changed toward transition regime gradually. O₃ formation regime in urban area was more likely to be VOC-limited regime, while regime in suburban area was more likely to be NO$_x$-limited. FNR$_{SAT}$ was corrected based on the hourly surface FNR and O₃ data to make it better to reflect O₃ formation in a day. After correcting

360 FNR$_{SAT}$ with seasonal correction coefficients of 0.85, 0.84, and 0.77 for spring, summer, and autumn respectively, O₃

formation regime in Shanghai was more inclined to VOC-limited in both time and spatial distribution, and the effectiveness of FNR$_{SAT}$ correction was confirmed by the surface observation. Thus, this correction is significant for using satellite data to improve the accuracy in indicating surface O_3 formation.

Data availability. Data are available for scientific purposes upon request to the corresponding author.

Author Contributions: DL and SW designed and implemented the research, and prepared the manuscript; RX contributed to the analysis of OMI products and MEIC inventory; JZ provided the HCHO and NO_2 data observed by LP-DOAS; SZ and ZS revised the manuscript; BZ provided constructive comments and supported the DOAS measurements.

Competing interests. The authors declare that they have no conflict of interest.

Acknowledgments: We acknowledge the free use of OMI HCHO and NO_2 products from NASA Goddard Earth Sciences (GES) Data and Information Services Center (DISC). We also thank Center for Earth System Science, Tsinghua University for MEIC data.

Financial support: This research was funded by National Key Research and Development Program of China (2017YFC0210002), National Natural Science Foundation of China (41775113, 21777026), and Funds for International Cooperation and Exchange of the National Natural Science Foundation of China (Grant No. 42061134006).

References

An, J. Y., Huang, Y. W., Huang, C., Wang, X., Yan, R. S., Wang, Q., Wang, H. L., Jing, S. A., Zhang, Y., Liu, Y. M., Chen, Y., Xu, C., Qiao, L. P., Zhou, M., Zhu, S. H., Hu, Q. Y., Lu, J., and Chen, C. H.: Emission inventory of air pollutants and chemical speciation for specific anthropogenic sources based on local measurements in the Yangtze River Delta region, China, Atmos Chem Phys, 21, 2003-2025, https://doi.org/10.5194/acp-21-2003-2021, 2021.

Bovensmann, H., Burrows, J. P., Buchwitz, M., Frerick, J., Noel, S., Rozanov, V. V., Chance, K. V., and Goede, A. P. H.: SCIAMACHY: Mission objectives and measurement modes, J Atmos Sci, 56, 127-150, https://doi.org/Doi 10.1175/1520-0469(1999)056<0127:Smoamm>2.0.Co;2, 1999.

Burrows, J. P., Weber, M., Buchwitz, M., Rozanov, V., Ladstatter-Weissenmayer, A., Richter, A., DeBeek, R., Hoogen, R., Bramstedt, K., Eichmann, K. U., and Eisinger, M.: The global ozone monitoring experiment (GOME): Mission concept and first scientific results, J Atmos Sci, 56, 151-175, https://doi.org/Doi 10.1175/1520-0469(1999)056<0151:Tgomeg>2.0.Co;2, 1999.

Callies, J., Corpaccioli, E., Eisinger, M., Hahne, A., and Lefebvre, A.: GOME-2 - Metop's second-generation sensor for operational ozone monitoring, Esa Bull-Eur Space, 28-36, 2000.

Chan, K. L., Wang, Z. R., Ding, A. J., Heue, K. P., Shen, Y. C., Wang, J., Zhang, F., Shi, Y. N., Hao, N., and Wenig, M.: MAX-DOAS measurements of tropospheric NO_2 and HCHO in Nanjing and a comparison to ozone monitoring instrument observations, Atmos Chem Phys, 19, 10051-10071, https://doi.org/10.5194/acp-19-10051-2019, 2019.

De Smedt, I., Van Roozendael, M., Stavrakou, T., Muller, J. F., Lerot, C., Theys, N., Valks, P., Hao, N., and van der A, R.: Improved retrieval of global tropospheric formaldehyde columns from GOME-2/MetOp-A addressing noise reduction and instrumental degradation issues, Atmos Meas Tech, 5, 2933-2949, https://doi.org/10.5194/amt-5-2933-2012, 2012.

400 Duncan, B. N., Yoshida, Y., Damon, M. R., Douglass, A. R., and Witte, J. C.: Temperature dependence of factors controlling isoprene emissions, Geophys Res Lett, 36, https://doi.org/10.1029/2008GL037090, 2009.

Duncan, B. N., Yoshida, Y., Olson, J. R., Sillman, S., Martin, R. V., Lamsal, L., Hu, Y. T., Pickering, K. E., Retscher, C., Allen, D. J., and Crawford, J. H.: Application of OMI observations to a space-based indicator of NO_x and VOC controls on surface ozone formation, Atmos Environ, 44, 2213-2223, https://doi.org/10.1016/j.atmosenv.2010.03.010, 2010.

405 Fan, J. C., Ju, T. Z., Wang, Q. H., Gao, H. Y., Huang, R. R., and Duan, J. L.: Spatiotemporal variations and potential sources of tropospheric formaldehyde over eastern China based on OMI satellite data, Atmos Pollut Res, 12, 272-285, https://doi.org/10.1016/j.apr.2020.09.011, 2021.

Gao, W., Tie, X. X., Xu, J. M., Huang, R. J., Mao, X. Q., Zhou, G. Q., and Chang, L. Y.: Long-term trend of O_3 in a mega City (Shanghai), China: Characteristics, causes, and interactions with precursors, Sci Total Environ, 603, 425-433,
410 https://doi.org/10.1016/j.scitotenv.2017.06.099, 2017.

Geng, F. H., Tie, X. X., Xu, J. M., Zhou, G. Q., Peng, L., Gao, W., Tang, X., and Zhao, C. S.: Characterizations of ozone, NO_x, and VOCs measured in Shanghai, China, Atmos Environ, 42, 6873-6883, https://doi.org/10.1016/j.atmosenv.2008.05.045, 2008.

Jin, X. M., and Holloway, T.: Spatial and temporal variability of ozone sensitivity over China observed from the Ozone
415 Monitoring Instrument, J. Geophys. Res.-Atmos., 120, 7229-7246, https://doi.org/10.1002/2015jd023250, 2015.

Jin, X. M., Fiore, A. M., Murray, L. T., Valin, L. C., Lamsal, L. N., Duncan, B., Folkert Boersma, K., De Smedt, I., Abad, G. G., Chance, K., and Tonnesen, G. S.: Evaluating a Space-Based Indicator of Surface Ozone-NO_x-VOC Sensitivity Over Midlatitude Source Regions and Application to Decadal Trends, J. Geophys. Res.-Atmos., 122, 10231-10253, https://doi.org/10.1002/2017jd026720, 2017.

420 Jin, X. M., Fiore, A., Boersma, K. F., De Smedt, I., and Valin, L.: Inferring Changes in Summertime Surface Ozone-NO_x-VOC Chemistry over US Urban Areas from Two Decades of Satellite and Ground-Based Observations, Environ Sci Technol, 54, 6518-6529, https://doi.org/10.1021/acs.est.9b07785, 2020.

Krotkov, N. A., McLinden, C. A., Li, C., Lamsal, L. N., Celarier, E. A., Marchenko, S. V., Swartz, W. H., Bucsela, E. J., Joiner, J., Duncan, B. N., Boersma, K. F., Veefkind, J. P., Levelt, P. F., Fioletov, V. E., Dickerson, R. R., He, H., Lu, Z.
425 F., and Streets, D. G.: Aura OMI observations of regional SO_2 and NO_2 pollution changes from 2005 to 2015, Atmos Chem Phys, 16, 4605-4629, https://doi.org/10.5194/acp-16-4605-2016, 2016.

Lee, H., Ryu, J., Irie, H., Jang, S. H., Park, J., Choi, W., and Hong, H.: Investigations of the Diurnal Variation of Vertical HCHO Profiles Based on MAX-DOAS Measurements in Beijing: Comparisons with OMI Vertical Column Data, Atmosphere-Basel, 6, 1816-1832, https://doi.org/10.3390/atmos6111816, 2015.

430 Levelt, P. F., Van den Oord, G. H. J., Dobber, M. R., Malkki, A., Visser, H., de Vries, J., Stammes, P., Lundell, J. O. V., and Saari, H.: The Ozone Monitoring Instrument, Ieee T Geosci Remote, 44, 1093-1101, https://doi.org/10.1109/Tgrs.2006.872333, 2006.

Li, K., Jacob, D. J., Liao, H., Shen, L., Zhang, Q., and Bates, K. H.: Anthropogenic drivers of 2013-2017 trends in summer surface ozone in China, P Natl Acad Sci USA, 116, 422-427, https://doi.org/10.1073/pnas.1812168116, 2019.

435 Li, X., Rohrer, F., Brauers, T., Hofzumahaus, A., Lu, K., Shao, M., Zhang, Y. H., and Wahner, A.: Modeling of HCHO and CHOCHO at a semi-rural site in southern China during the PRIDE-PRD2006 campaign, Atmos Chem Phys, 14, 12291-12305, https://doi.org/10.5194/acp-14-12291-2014, 2014.

Ling, Z. H., Guo, H., Chen, G. X., Lam, S. H. M., and Fan, S. J.: Formaldehyde and Acetaldehyde at Different Elevations in Mountainous Areas in Hong Kong, Aerosol Air Qual Res, 16, 1868-1878, https://doi.org/10.4209/aaqr.2015.09.0571,
440 2016.

Liu, H. R., Liu, C., Xie, Z. Q., Li, Y., Huang, X., Wang, S. S., Xu, J., and Xie, P. H.: A paradox for air pollution controlling in China revealed by "APEC Blue" and "Parade Blue", Sci Rep-Uk, 6, 13, https://doi.org/10.1038/srep34408, 2016.

Liu, R., Feng, T., Wang, S. S., Shi, C. Z., Guo, Y. L., Nan, J. L., Deng, Y., and Zhou, B.: OMI satellite observed formaldehyde column from 2006 to 2015 over Xishuangbanna, southwest China, and validation using ground based
445 zenith-sky DOAS, Sci Total Environ, 613, 168-175, https://doi.org/10.1016/j.scitotenv.2017.08.210, 2018a.

Liu, Y., Li, L., An, J., Zhang, W., Yan, R., Huang, L., Huang, C., Wang, H., Wang, Q., and Wang, M.: Emissions, Chemical Composition, and Spatial and Temporal Allocation of the BVOCs in the Yangtze River Delta Region in 2014, ENVIRONMENTAL SCIENCE, 39, 608-617, 2018b.

450   Liu, Y., Li, L., An, J. Y., Huang, L., Yan, R. S., Huang, C., Wang, H. L., Wang, Q., Wang, M., and Zhang, W.: Estimation of biogenic VOC emissions and its impact on ozone formation over the Yangtze River Delta region, China, Atmos Environ, 186, 113-128, https://doi.org/10.1016/j.atmosenv.2018.05.027, 2018c.

Liu, Y., Tang, Z. P., Abera, T., Zhang, X. Z., Hakola, H., Pellikka, P., and Maeda, E.: Spatio-temporal distribution and source partitioning of formaldehyde over Ethiopia and Kenya, Atmos Environ, 237, 9, https://doi.org/10.1016/j.atmosenv.2020.117706, 2020.

455   Luo, H. H., Yang, L. F., Yuan, Z. B., Zhao, K. H., Zhang, S., Duan, Y. S., Huang, R. Z., and Fu, Q. Y.: Synoptic condition-driven summertime ozone formation regime in Shanghai and the implication for dynamic ozone control strategies, Sci Total Environ, 745, 12, https://doi.org/10.1016/j.scitotenv.2020.141130, 2020.

Marais, E. A., Jacob, D. J., Kurosu, T. P., Chance, K., Murphy, J. G., Reeves, C., Mills, G., Casadio, S., Millet, D. B., Barkley, M. P., Paulot, F., and Mao, J.: Isoprene emissions in Africa inferred from OMI observations of formaldehyde columns, Atmos Chem Phys, 12, 6219-6235, https://doi.org/10.5194/acp-12-6219-2012, 2012.

460   Martin, R. V., Fiore, A. M., and Van Donkelaar, A.: Space-based diagnosis of surface ozone sensitivity to anthropogenic emissions, Geophys Res Lett, 31, L06120 06121-06124, https://doi.org/10.1029/2004gl019416, 2004a.

Martin, R. V., Parrish, D. D., Ryerson, T. B., Nicks, D. K., Chance, K., Kurosu, T. P., Jacob, D. J., Sturges, E. D., Fried, A., and Wert, B. P.: Evaluation of GOME satellite measurements of tropospheric NO_2 and HCHO using regional data from

465   aircraft campaigns in the southeastern United States, J. Geophys. Res.-Atmos., 109, 11, https://doi.org/10.1029/2004jd004869, 2004b.

Miller, C. C., Jacob, D. J., Marais, E. A., Yu, K. R., Travis, K. R., Kim, P. S., Fisher, J. A., Zhu, L., Wolfe, G. M., Hanisco, T. F., Keutsch, F. N., Kaiser, J., Min, K. E., Brown, S. S., Washenfelder, R. A., Abad, G. G., and Chance, K.: Glyoxal yield from isoprene oxidation and relation to formaldehyde: chemical mechanism, constraints from SENEX aircraft

470   observations, and interpretation of OMI satellite data, Atmos Chem Phys, 17, 8725-8738, https://doi.org/10.5194/acp-17-8725-2017, 2017.

Millet, D. B., Jacob, D. J., Boersma, K. F., Fu, T. M., Kurosu, T. P., Chance, K., Heald, C. L., and Guenther, A.: Spatial distribution of isoprene emissions from North America derived from formaldehyde column measurements by the OMI satellite sensor, J. Geophys. Res.-Atmos., 113, 18, https://doi.org/10.1029/2007jd008950, 2008.

475   Narumi, D., Kondo, A., and Shimoda, Y.: The effect of the increase in urban temperature on the concentration of photochemical oxidants, Atmos Environ, 43, 2348-2359, https://doi.org/10.1016/j.atmosenv.2009.01.028, 2009.

Palmer, P. I., Abbot, D. S., Fu, T. M., Jacob, D. J., Chance, K., Kurosu, T. P., Guenther, A., Wiedinmyer, C., Stanton, J. C., Pilling, M. J., Pressley, S. N., Lamb, B., and Sumner, A. L.: Quantifying the seasonal and interannual variability of North American isoprene emissions using satellite observations of the formaldehyde column, J. Geophys. Res.-Atmos.,

480   111, 14, https://doi.org/10.1029/2005jd006689, 2006.

Pang, X. B., Mu, Y. J., Lee, X. Q., Zhang, Y. J., and Xu, Z.: Influences of characteristic meteorological conditions on atmospheric carbonyls in Beijing, China, Atmos Res, 93, 913-919, https://doi.org/10.1016/j.atmosres.2009.05.001, 2009.

Schroeder, J. R., Crawford, J. H., Fried, A., Walega, J., Weinheimer, A., Wisthaler, A., Muller, M., Mikoviny, T., Chen, G., Shook, M., Blake, D. R., and Tonnesen, G. S.: New insights into the column CH_2O/NO_2 ratio as an indicator of near-

485   surface ozone sensitivity, J. Geophys. Res.-Atmos., 122, 8885-8907, https://doi.org/10.1002/2017jd026781, 2017.

Sharkey, T. D., and Loreto, F.: Water-stress, temperature, and light effects on the capacity for isoprene emission and photosynthesis of kudzu leaves, Oecologia, 95, 328-333, https://doi.org/10.1007/bf00320984, 1993.

Shen, L., Jacob, D. J., Zhu, L., Zhang, Q., Zheng, B., Sulprizio, M. P., Li, K., De Smedt, I., Abad, G. G., Cao, H. S., Fu, T. M., and Liao, H.: The 2005-2016 Trends of Formaldehyde Columns Over China Observed by Satellites: Increasing

490   Anthropogenic Emissions of Volatile Organic Compounds and Decreasing Agricultural Fire Emissions, Geophys Res Lett, 46, 4468-4475, https://doi.org/10.1029/2019gl082172, 2019.

Sillman, S.: The use of NO_y, H_2O_2, and HNO_3 as indicators for Ozone-NO_x-Hydrocarbon sensitivity in Urban Locations, J. Geophys. Res.-Atmos., 100, 14175-14188, https://doi.org/doi 10.1029/94jd02953, 1995.

Souri, A. H., Choi, Y., Jeon, W., Woo, J. H., Zhang, Q., and Kurokawa, J.: Remote sensing evidence of decadal changes in major tropospheric ozone precursors over East Asia, J. Geophys. Res.-Atmos., 122, 2474-2492, https://doi.org/10.1002/2016jd025663, 2017.

Stavrakou, T., Muller, J. F., De Smedt, I., Van Roozendael, M., van der Werf, G. R., Giglio, L., and Guenther, A.: Global emissions of non-methane hydrocarbons deduced from SCIAMACHY formaldehyde columns through 2003-2006, Atmos Chem Phys, 9, 3663-3679, https://doi.org/10.5194/acp-9-3663-2009, 2009.

Su, W. J., Liu, C., Hu, Q. H., Zhao, S. H., Sun, Y. W., Wang, W., Zhu, Y. Z., Liu, J. G., and Kim, J.: Primary and secondary sources of ambient formaldehyde in the Yangtze River Delta based on Ozone Mapping and Profiler Suite (OMPS) observations, Atmos Chem Phys, 19, 6717-6736, https://doi.org/10.5194/acp-19-6717-2019, 2019.

Veefkind, J. P., Aben, I., McMullan, K., Forster, H., de Vries, J., Otter, G., Claas, J., Eskes, H. J., de Haan, J. F., Kleipool, Q., van Weele, M., Hasekamp, O., Hoogeveen, R., Landgraf, J., Snel, R., Tol, P., Ingmann, P., Voors, R., Kruizinga, B., Vink, R., Visser, H., and Levelt, P. F.: TROPOMI on the ESA Sentinel-5 Precursor: A GMES mission for global observations of the atmospheric composition for climate, air quality and ozone layer applications, Remote Sens Environ, 120, 70-83, https://doi.org/10.1016/j.rse.2011.09.027, 2012.

Vigouroux, C., Langerock, B., Aquino, C. A. B., Blumenstock, T., Cheng, Z. B., De Maziere, M., De Smedt, I., Grutter, M., Hannigan, J. W., Jones, N., Kivi, R., Loyola, D., Lutsch, E., Mahieu, E., Makarova, M., Metzger, J. M., Morino, I., Murata, I., Nagahama, T., Notholt, J., Ortega, I., Palm, M., Pinardi, G., Rohling, A., Smale, D., Stremme, W., Strong, K., Sussmann, R., Te, Y., van Roozendael, M., Wang, P. C., and Winkler, H.: TROPOMI-Sentinel-5 Precursor formaldehyde validation using an extensive network of ground-based Fourier-transform infrared stations, Atmos Meas Tech, 13, 3751-3767, https://doi.org/10.5194/amt-13-3751-2020, 2020.

Wang, T., Wang, P. C., Theys, N., Tong, D., Hendrick, F., Zhang, Q., and Van Roozendael, M.: Spatial and temporal changes in SO$_2$ regimes over China in the recent decade and the driving mechanism, Atmos Chem Phys, 18, 18063-18078, https://doi.org/10.5194/acp-18-18063-2018, 2018.

Wang, Y., Beirle, S., Lampel, J., Koukouli, M., De Smedt, I., Theys, N., Li, A., Wu, D. X., Xie, P. H., Liu, C., Van Roozendael, M., Stavrakou, T., Muller, J. F., and Wagner, T.: Validation of OMI, GOME-2A and GOME-2B tropospheric NO$_2$, SO$_2$ and HCHO products using MAX-DOAS observations from 2011 to 2014 in Wuxi, China: investigation of the effects of priori profiles and aerosols on the satellite products, Atmos Chem Phys, 17, 5007-5033, https://doi.org/10.5194/acp-17-5007-2017, 2017.

Wang, Y. P., Wang, Z. F., Yu, C., Zhu, S. Y., Cheng, L. X., Zhang, Y., and Chen, L. F.: Validation of OMI HCHO Products Using MAX-DOAS observations from 2010 to 2016 in Xianghe, Beijing: Investigation of the Effects of Aerosols on Satellite Products, Remote Sens-Basel, 11, 21, https://doi.org/10.3390/rs11020203, 2019.

Xing, C. Z., Liu, C., Hu, Q. H., Fu, Q. Y., Lin, H., Wang, S. T., Su, W. J., Wang, W. W., Javed, Z., and Liu, J. G.: Identifying the wintertime sources of volatile organic compounds (VOCs) from MAX-DOAS measured formaldehyde and glyoxal in Chongqing, southwest China, Sci Total Environ, 715, 12, https://doi.org/10.1016/j.scitotenv.2019.136258, 2020.

Xu, J. M., Tie, X. X., Gao, W., Lin, Y. F., and Fu, Q. Y.: Measurement and model analyses of the ozone variation during 2006 to 2015 and its response to emission change in megacity Shanghai, China, Atmos Chem Phys, 19, 9017-9035, https://doi.org/10.5194/acp-19-9017-2019, 2019.

Xue, R. B., Wang, S. S., Li, D. R., Zou, Z., Chan, K. L., Valks, P., Saiz-Lopez, A., and Zhou, B.: Spatio-temporal variations in NO$_2$ and SO$_2$ over Shanghai and Chongming Eco-Island measured by Ozone Monitoring Instrument (OMI) during 2008-2017, J Clean Prod, 258, 14, https://doi.org/10.1016/j.jclepro.2020.120563, 2020.

Zaveri, R. A., Berkowitz, C. M., Kleinman, L. I., Springston, S. R., Doskey, P. V., Lonneman, W. A., and Spicer, C. W.: Ozone production efficiency and NO$_x$ depletion in an urban plume: Interpretation of field observations and implications for evaluating O$_3$-NO$_x$-VOC sensitivity, J. Geophys. Res.-Atmos., 108, 23, https://doi.org/10.1029/2002jd003144, 2003.

Zhang, C. X., Liu, C., Hu, Q. H., Cai, Z. N., Su, W. J., Xia, C. Z., Zhu, Y. Z., Wang, S. W., and Liu, J. G.: Satellite UV-Vis spectroscopy: implications for air quality trends and their driving forces in China during 2005-2017, Light-Sci Appl, 8, 12, https://doi.org/10.1038/s41377-019-0210-6, 2019.

Zhang, K., Li, L., Huang, L., Wang, Y. J., Huo, J. T., Duan, Y. S., Wang, Y. H., and Fu, Q. Y.: The impact of volatile organic compounds on ozone formation in the suburban area of Shanghai, Atmos Environ, 232, 11, https://doi.org/10.1016/j.atmosenv.2020.117511, 2020.

Zhang, K., Huang, L., Li, Q., Huo, J. T., Duan, Y. S., Wang, Y. H., Yaluk, E., Wang, Y. J., Fu, Q. Y., and Li, L.: Explicit
545   modeling of isoprene chemical processing in polluted air masses in suburban areas of the Yangtze River Delta region: radical cycling and formation of ozone and formaldehyde, Atmos Chem Phys, 21, 5905-5917, https://doi.org/10.5194/acp-21-5905-2021, 2021.

Zhang, Q., Streets, D. G., He, K., Wang, Y., Richter, A., Burrows, J. P., Uno, I., Jang, C. J., Chen, D., Yao, Z., and Lei, Y.: NO_x emission trends for China, 1995-2004: The view from the ground and the view from space, J. Geophys. Res.-
550   Atmos., 112, 18, https://doi.org/10.1029/2007jd008684, 2007.

Zhu, L., Jacob, D. J., Keutsch, F. N., Mickley, L. J., Scheffe, R., Strum, M., Abad, G. G., Chance, K., Yang, K., Rappengluck, B., Millet, D. B., Baasandorj, M., Jaegle, L., and Shah, V.: Formaldehyde (HCHO) As a Hazardous Air Pollutant: Mapping Surface Air Concentrations from Satellite and Inferring Cancer Risks in the United States, Environ Sci Technol, 51, 5650-5657, https://doi.org/10.1021/acs.est.7b01356, 2017a.

555 Zhu, L., Mickley, L. J., Jacob, D. J., Marais, E. A., Sheng, J. X., Hu, L., Abad, G. G., and Chance, K.: Long-term (2005-2014) trends in formaldehyde (HCHO) columns across North America as seen by the OMI satellite instrument: Evidence of changing emissions of volatile organic compounds, Geophys Res Lett, 44, 7079-7086, https://doi.org/10.1002/2017gl073859, 2017b.